metals

MDPI

Article

# Phase Evolution of the $Al_xNbTiVZr$ ($x$ = 0; 0.5; 1; 1.5) High Entropy Alloys

**Nikita Y. Yurchenko [1], Nikita D. Stepanov [1,*], Mikhail A. Tikhonovsky [2] and Gennady A. Salishchev [1]**

[1] Laboratory of Bulk Nanostructured Materials, Belgorod National Research University, Belgorod 308015, Russia; yurchenko_nikita@bsu.edu.ru (N.Y.Y.); salishchev@bsu.edu.ru (G.A.S.)

[2] National Science Center, Kharkov Institute of Physics and Technology, NAS of Ukraine, Kharkov 61108, Ukraine; tikhonovsky@kipt.kharkov.ua

* Correspondence: stepanov@bsu.edu.ru; Tel.: +7-4722-585-416

Academic Editor: Michael C. Gao

Received: 26 October 2016; Accepted: 21 November 2016; Published: 25 November 2016

**Abstract:** $Al_xNbTiVZr$ ($x$ = 0; 0.5; 1; 1.5) high entropy alloys were fabricated by vacuum arc melting and annealed at 1200 °C for 24 h. The NbTiVZr alloy had single body centered cubic (bcc) solid solution phase after annealing at 1200 °C, while, in the Al-containing alloys, C14 Laves and $Zr_2Al$-type phases are found. The alloys were subjected to annealing at 800 °C and 1000 °C. It was shown that annealing temperature (800 °C or 1000 °C) weakly affected the produced phases but the Al content had pronounced effect on structure of the annealed alloys. The NbTiVZr alloy decomposed into bcc, Zr-rich hexagonal close-packed (hcp), and C15 Laves phases. In the $Al_{0.5}NbTiVZr$ alloy, the bcc matrix phase also decomposed into a mixture of bcc and C14 Laves phases. In the AlNbTiVZr alloy, annealing resulted in an increase of volume fraction of $Zr_2Al$-type phase. Finally, in the $Al_{1.5}NbTiVZr$ alloy, formation of $AlNb_2$-type phase was observed. The highest fraction of second phases appeared after annealing in the NbTiVZr alloy. It is demonstrated that the strong chemical affinity and high enthalpy of formation of intermetallic phases in Al-Zr atomic pair govern the intermetallic phase formation in the alloys at 1200 °C. Increase of volume fraction of second phases in the alloys due to annealing at 800 °C and 1000 °C is in proportion to the decrease of Zr concentration in the bcc matrix phase.

**Keywords:** high-entropy alloys; microstructure; phase stability; second phases

## 1. Introduction

In the recent decade, the so-called high-entropy alloys (HEAs)—alloys, usually defined as multicomponent alloys consisting of at least five principal elements with nearly equimolar concentrations—have attracted considerable attention from materials scientists worldwide, mostly due to the attractive properties of the alloys [1]. The "high entropy" term originates from the high mixing entropy of the multicomponent equiatomic random solid solution phases in the alloys, which is believed to make the formation of the solid solution phases more thermodynamically preferred than the intermetallic ones [2]. Many alloys with attractive properties, such as high room temperature strength [3–5], extraordinary fracture or impact toughness [6–8], and high wear resistance [9] were reported. One of the particularly attractive properties, demonstrated by some HEAs, is a high strength at elevated temperatures, which makes them promising materials for high-temperature applications, which are required in, for example, aerospace industry [10–15].

The HEAs intended for high-temperature usage are usually composed of solely heavy and ultra-refractory elements such as Mo, Hf, Ta and W [16,17], or some lighter elements with lower melting temperatures such as Cr, Nb, Ti, V, and Zr are added [18–24]. Many of the alloys also

contain other elements, for example, Al [13–15,25–33]. The addition of Al has beneficial effects including: (i) reduction of density [25,27,28]; (ii) increase of strength both at room and elevated temperatures [14,25,26,28]; and (iii) increased oxidation resistance [31]. However, there is diverse information on effect of Al on phase composition of refractory HEAs: in many cases, Al stabilizes solid solution phases [25,29,31], but it can also stabilize intermetallic phases [27,32]. The reasons for different effect of Al on phase composition of the refractory element based alloys deserve additional studies.

Another poorly studied aspect of refractory HEAs is their phase stability. Usually, the structure of the alloys is reported either in as-solidified condition or after homogenization heat treatment at very high temperatures (1200–1400 °C) [12–33]. Sometimes, structure after plastic deformation at lower temperatures (600–1200 °C) is also examined [12–14,19,20,23,25,33], but relatively short high-temperature exposure times during mechanical testing may not be sufficient to produce equilibrium phases in the tested alloy [14]. If the alloy exhibits phase transformations at temperatures below the homogenization temperature, the long high-temperature exposure can result in the drastic changes in microstructure and resulting mechanical properties. Therefore, it is necessary to examine the phase evolution of refractory HEAs at temperatures corresponding to potential operation temperatures. Unfortunately, at the moment, only a few reports on the effect of annealing treatment on phase composition and microstructure of refractory HEAs are available [30,34,35].

In this work, we have investigated the effect of annealing at 800 °C and 1000 °C on structure of the $Al_xNbTiVZr$ ($x$ = 0; 0.5; 1; 1.5) high entropy alloys. Prior to annealing at intermediate temperatures (800 °C and 1000 °C), the alloys were annealed at 1200 °C for 24 h to produce equilibrium high-temperature phases. The preliminary results on structure of the alloys in as-solidified and annealed (1200 °C, 24 h) conditions, as well as room temperature mechanical properties and densities, were reported elsewhere [27]. It was found that increase of Al content results in formation and increase of volume fraction of second phases. The aims of current work can be summarized as the following: (i) to better understand Al effect on phase formation in refractory HEAs; and (ii) to estimate phase stability of the $Al_xNbTiVZr$ ($x$ = 0; 0.5; 1; 1.5) alloys.

## 2. Materials and Methods

The alloys with a nominal composition of NbTiVZr, $Al_{0.5}NbTiVZr$, AlNbTiVZr and $Al_{1.5}NbTiVZr$ were produced by arc melting of the elements in a low-pressure, high-purity argon atmosphere inside a water-cooled copper cavity. The purities of the alloying elements were above 99.9 at. %. The produced ingots of the alloys had dimensions of about 6 × 12 × 40 $mm^3$. As-solidified ingots were annealed at 1200 °C for 24 h. This annealing treatment corresponds to the homogenization regime previously developed for the NbTiVZr alloy [21]. Prior to annealing, the samples were sealed in vacuumed ($10^{-2}$ torr) quartz tubes filled with titanium chips to prevent oxidation.

Rectangular specimens with a thickness of ≈3 mm and length and width of ≈5–7 mm were cut using the electric discharge machine from the annealed at 1200 °C specimens. These specimens were annealed at 800 °C and 1000 °C for 100 h. Prior to annealing, the samples were sealed in vacuumed ($10^{-2}$ torr) quartz tubes filled with titanium chips to prevent oxidation. Then the samples were put into preheated furnace and held for 100 h. Cooling after the annealing was carried out in laboratory air.

Structure of the alloys was studied using X-ray diffraction (XRD) and scanning electron microscopy (SEM) techniques. The XRD analysis was performed using ULTIMA IV diffractometer (Rigaku Corporation, Tokyo, Japan) and Cu K$\alpha$ radiation. The analysis of XRD data was performed using PowderCell software (W. Krauss & G. Nolze, Berlin, Germany) and NIMS Materials Database (NIMS, Tsukuba, Japan). Samples for SEM observations were prepared by careful mechanical polishing. SEM investigations were performed utilizing FEI Quanta 600 FEG or Nova NanoSEM microscopes (FEI Company, Hillsboro, OR, USA) equipped with back-scattered electron (BSE), energy-dispersive spectrometry (EDS), and electron backscattered diffraction (EBSD) detectors. The dimensions of second phase particles were measured from SEM-BSE images using the linear intercept method with Digimizer Image Analysis Software (MedCalc Software, Bruges, Belgium). The volume fraction of

different phases was also measured using the same software by binarization procedure and subsequent area analysis.

## 3. Results

### *3.1. Structure of the $Al_xNbTiVZr$ (x = 0; 0.5; 1; 1.5) Alloys after Annealing at 1200 °C*

Figure 1 shows the XRD patterns of the $Al_xNbTiVZr$ alloys after annealing at 1200 °C. The NbTiVZr alloy has single body centered cubic (bcc) phase. One can note the splitting of the bcc peaks. The reasons for the splitting are unknown at the moment and require additional studies. In the $Al_{0.5}NbTiVZr$ alloy, alongside with the reflections from bcc lattice, stronger peaks from hexagonal (C14) Laves phase and weaker peaks of hexagonal $Zr_2Al$ phase are observed. In the AlNbTiVZr and $Al_{1.5}NbTiVZr$ alloys with higher Al concentration intensity of Bragg peaks from both Laves and $Zr_2Al$ phases increases and intensity of peaks from bcc lattice decreases.

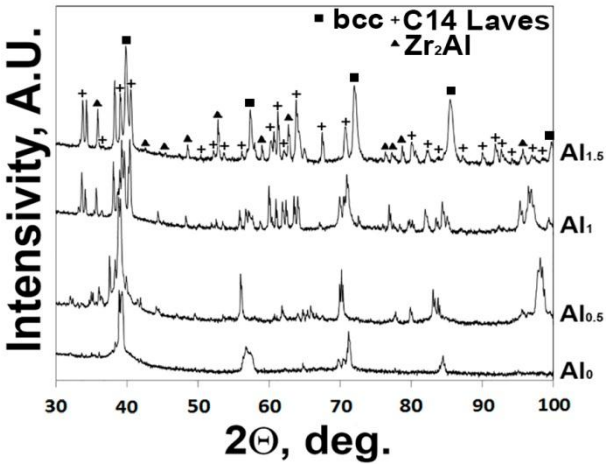


**Figure 1.** XRD patterns of the $Al_xNbTiVZr$ ($x$ = 0; 0.5; 1; 1.5) alloys after annealing at 1200 °C for 24 h.

Microstructure of the $Al_xNbTiVZr$ alloys after annealing at 1200 °C is shown in Figure 2. The chemical composition of the constitutive phases and their volume fractions are given in Table 1. The NbTiVZr alloy has coarse-grained single phase structure (Figure 2a). The chemical composition of the apparently bcc grains corresponds to the actual chemical composition of the alloy (Table 1). However, very thin layer of a second phase on a grain boundary can be seen in higher magnification insert in Figure 2a.

The $Al_{0.5}NbTiVZr$ alloy (Figure 2b) is composed of the bcc matrix (point 1) and second phase particles of two types: dark-grey Laves phase particles (point 2) and light $Zr_2Al$-type ones (point 3) [27]. The crystal structure of the phases was verified by EBSD patterns. The individual Laves phase particles are usually found on grain boundaries. The light $Zr_2Al$-type particles are mostly adjacent to Laves phase particles. The average size of the particles is about 5–20 μm. The volume fractions of Laves and $Zr_2Al$-type phases are 14% and 3% respectively. The bcc grains have composition reasonably close to the actual composition of the alloy (Table 1). Laves phase is enriched with Zr, V and Al. The composition of $Zr_2Al$-type phase is similar to that of Laves phase, but the concentration of Zr is considerably higher and the concentration of V is considerably lower in the $Zr_2Al$-type phase than in the Laves phase particles.

The microstructures of the AlNbTiVZr (Figure 2c) and the $Al_{1.5}NbTiVZr$ (Figure 2d) alloys are similar to that of the $Al_{0.5}NbTiVZr$ alloy (Figure 2b). The same constitutive phases, namely the bcc matrix (point 1, Figure 2c, d), the dark-grey Laves particles (point 2) and the $Zr_2Al$-type phase light particles (point 3) are observed. The volume fractions of the Laves and $Zr_2Al$-type phase particles in the AlNbTiVZr alloy are 21% and 12%, respectively. The respective values for the $Al_{1.5}NbTiVZr$ alloy

are 16% and 30%. Chemical analysis (Table 1) demonstrates that the bcc phase is enriched with Nb and Ti and depleted of Zr and Al. The dark-grey Laves particles, in turn, mainly consist from Zr, Al and V, and the light $Zr_2Al$-type particles are enriched of Zr and Al.

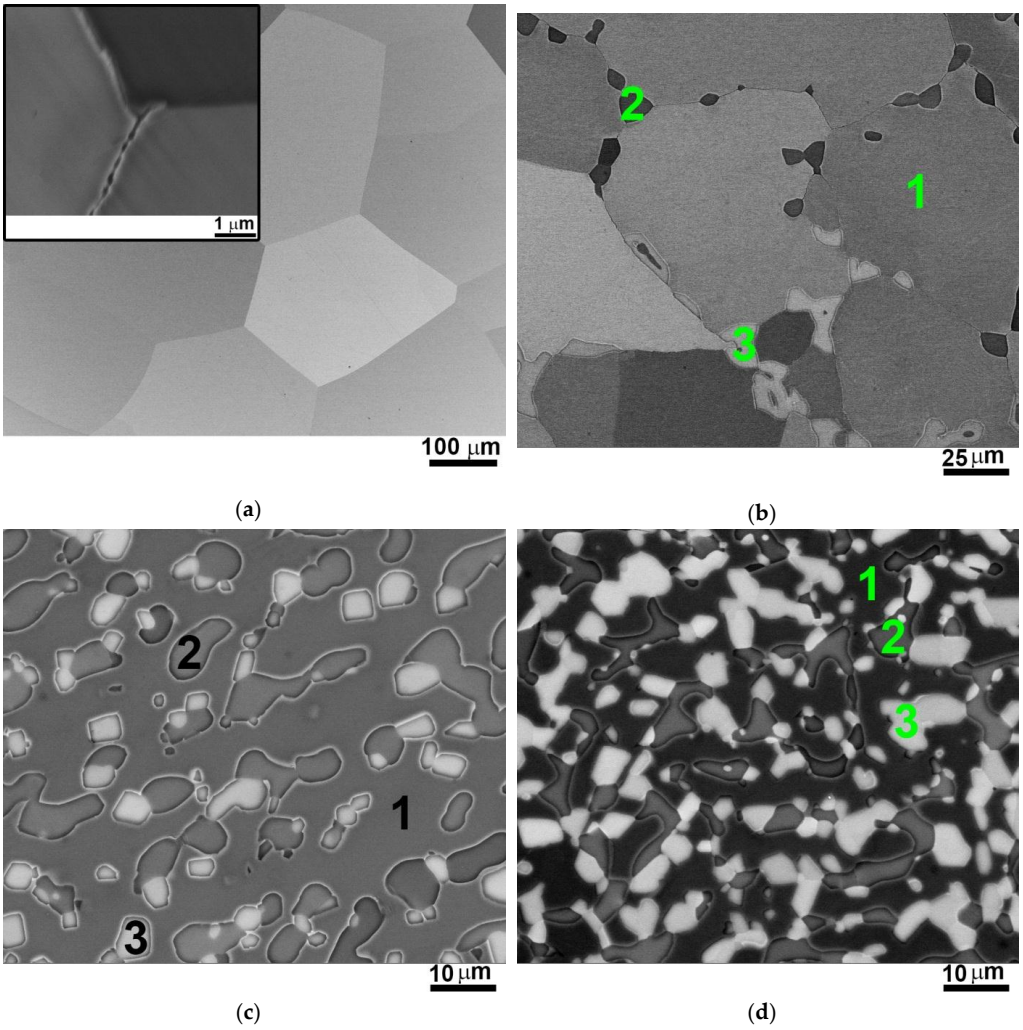


**Figure 2.** SEM-BSE images of the microstructures of the $Al_xNbTiVZr$ ($x$ = 0 (**a**); 0.5 (**b**); 1 (**c**); 1.5 (**d**)) alloys after annealing at 1200 °C for 24 h. Chemical compositions and volume fractions of the numbered constituents are given in Table 1.

**Table 1.** Chemical compositions, volume fractions and dimensions of the constituents of the $Al_xNbTiVZr$ ($x$ = 0; 0.5; 1; 1.5) alloys after annealing at 1200 °C for 24 h. Typical regions used for analysis are shown in Figure 2.

| | Element, at. % | Al | Nb | Ti | V | Zr | Volume Fraction, % | Average Size, μm | |
|---|---|---|---|---|---|---|---|---|---|
| | | | | | | | | Transversal | Longitudinal |
| No. | Constituents Designation | | | | | | NbTiVZr | | |
| 1 | Grains | - | 25.6 | 25.5 | 24.9 | 24.0 | 100 | 240 ± 100 | |
| | Alloy composition | - | 25.6 | 24.4 | 24.9 | 25.1 | - | - | |
| | | | | | | | $Al_{0.5}NbTiVZr$ | | |
| 1 | Matrix | 9.5 | 25.8 | 24.7 | 20.8 | 19.2 | 83 ± 3 | 50 ± 25 | |
| 2 | Dark-grey particles | 19.5 | 11.6 | 8.6 | 28.3 | 32.0 | 14 ± 2 | 7.9 ± 4.2 | |
| 3 | Light-grey particles | 17.3 | 9.1 | 12.5 | 20.0 | 41.1 | 3 ± 1 | 8.2 ± 3.0 | |
| | Alloy composition | 11.4 | 21.6 | 21.9 | 22.3 | 22.8 | - | - | |

**Table 1.** *Cont.*

| | Element, at. % | Al | Nb | Ti | V | Zr | Volume Fraction, % | Average Size, μm | |
|---|---|---|---|---|---|---|---|---|---|
| | | | | | | | | Transversal | Longitudinal |
| | | | | | AlNbTiVZr | | | | |
| 1 | Matrix | 16.5 | 25.8 | 24.7 | 18.5 | 14.5 | 67 ± 2 | - | |
| 2 | Dark-grey particles | 28.9 | 9.9 | 8.6 | 22.3 | 30.3 | 21 ± 3 | 5.3 ± 2.1 | 14.9 ± 7.3 |
| 3 | Light-grey particles | 38.7 | 9.5 | 8.3 | 3.6 | 39.9 | 12 ± 2 | 4.5 ± 1.3 | 8.1 ± 3.1 |
| | Alloy composition | 21.9 | 20.0 | 19.8 | 20.3 | 18.0 | - | - | |
| | | | | | $Al_{1.5}$NbTiVZr | | | | |
| 1 | Dark phase | 24.5 | 24.9 | 24.7 | 17.6 | 8.3 | 54 ± 3 | - | |
| 2 | Dark-grey phase | 36.2 | 7.9 | 7.6 | 19.9 | 28.4 | 16 ± 2 | 3.3 ± 1.1 | 8.1 ± 3.2 |
| 3 | Light-grey phase | 39.4 | 11.2 | 9 | 4.1 | 36.3 | 30 ± 2 | 3.8 ± 1.3 | |
| | Alloy composition | 29.5 | 18.0 | 18.2 | 16.9 | 17.4 | - | - | |

### 3.2. Effect of Annealing at 1000 °C on Structure of the $Al_xNbTiVZr$ ($x$ = 0; 0.5; 1; 1.5) Alloys

Figure 3 present results of XRD investigations of the $Al_xNbTiVZr$ ($x$ = 0; 0.5; 1; 1.5) alloys after annealing at 1000 °C. The NbTiVZr alloy is composed of primary bcc phase, and secondary cubic (C15) Laves and hexagonal close-packed (hcp) phases. The Al-containing alloys are composed of bcc phase, C14 Laves phase and $Zr_2Al$-type phase. Additional $AlNb_2$-type sigma phase is observed in the $Al_{1.5}$NbTiVZr alloy.

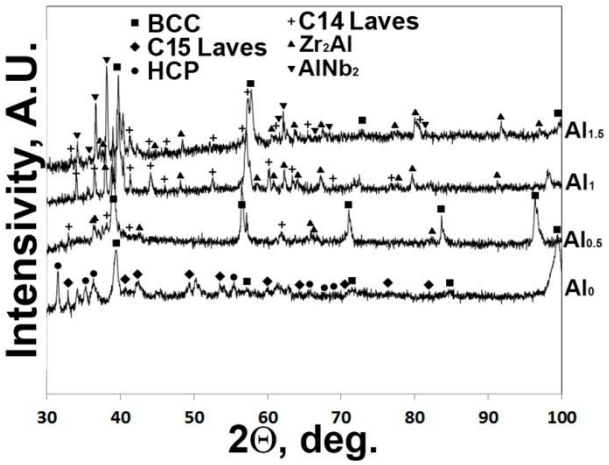


**Figure 3.** XRD patterns of the $Al_xNbTiVZr$ ($x$ = 0; 0.5; 1; and 1.5) alloys after annealing at 1000 °C for 100 h.

Figure 4 and Table 2 summarize data on structure of the $Al_xNbTiVZr$ ($x$ = 0, 0.5, 1, 1.5) alloys after annealing at 1000 °C for 100 h. The constitutive phases of the NbTiVZr alloy after annealing at 1000 °C (Figure 4a) are the light matrix phase (point 1 in Figure 4a), grey second phase particles (point 2) and black second phase particles (point 3). The results of local EDS and EBSD analysis show the matrix has bcc structure and is composed primary of Nb and V, the grey particles have hcp lattice and are based on Zr, while the black particles are (ordered Laves) fcc and are based on Ti (Table 2). The coarse grey hcp particles tend to have elongated morphology and width of ≈3 μm, and the fine black fcc Laves particles can be mostly found either inside the hcp particles or on the bcc/hcp interphases. Some individual Laves particles are also found in the matrix phase. The matrix, grey hcp and black Laves phases have volume fractions of 46%, 35% and 19%, respectively.

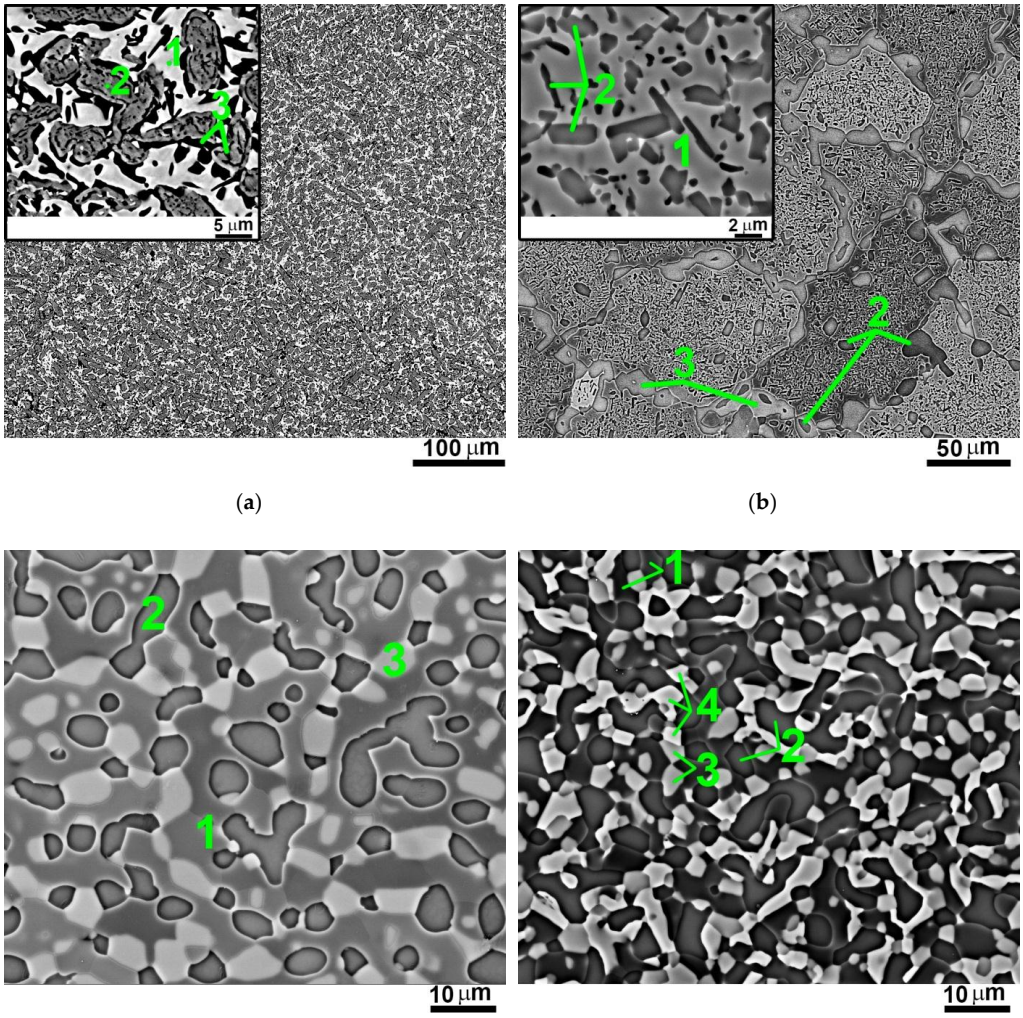


**Figure 4.** SEM-BSE images of the microstructures of the $Al_xNbTiVZr$ ($x$ = 0 (**a**); 0.5 (**b**); 1 (**c**); 1.5 (**d**)) alloys after annealing at 1000 °C for 100 h. Chemical compositions and volume fractions of the numbered constituents are given in Table 2.

Microstructure of the $Al_{0.5}NbTiVZr$ alloy after annealing at 1000 °C (Figure 4b) is composed of matrix bcc phase (point 1 in Figure 4b), dark-grey C14 Laves (point 2) and light-grey $Zr_2Al$-type (point 3) second phase particles. The chemical composition of the phases (Table 2) is close to that after annealing at 1200 °C (Table 2). The light-grey $Zr_2Al$-type particles can be found as coarse particles located on matrix grain boundaries. In turn, the dark-grey Laves phase particles are found both as coarse individual particle inside bcc grains and particles on grain boundaries, and also as very fine particles located predominantly on matrix-$Zr_2Al$ particle interphases. The volume fractions of respective Laves and $Zr_2Al$-type phases are 39% (4% of coarse and 35% of fine particles) and 13%, respectively.

Annealing of the equiatomic AlNbTiVZr alloy at 1000 °C (Figure 4c) does not result in substantial changes: the phase composition and morphology of the microstructure are close to that of the 1200 °C annealed (Figure 2c) alloy, yet the volume fraction of $Zr_2Al$-type phase increases noticeably to 22% (Table 2). The microstructure of the $Al_{1.5}NbTiVZr$ alloy after annealing at 1000 °C for 100 h (Figure 4d) becomes more complicated than after annealing at 1200 °C (Figure 2d): four phases with different contrast in SEM-BSE images are observed. Careful analysis using EDS and EBSD information has allowed identifying: (i) bcc phase (point 1 in Figure 4d); (ii) dark-grey C14 Laves phase (point 2);

(iii) light-grey $Zr_2Al$-type phase (point 3); and (iv) white $AlNb_2$-type phase with tetragonal lattice. The phases are found as individual particles with average sizes of around several micrometers. Chemical analysis shows that $AlNb_2$-type phase particles are enriched with Al and Nb (Table 2). The volume fractions of bcc, C14 Laves, $Zr_2Al$-type, and $AlNb_2$-type phases are, respectively, 36%, 28%, 16% and 20%.

**Table 2.** Chemical compositions, volume fractions and dimensions of the constituents of the $Al_xNbTiVZr$ ($x$ = 0; 0.5; 1; 1.5) alloys after annealing at 1000 °C for 100 h. Typical regions used for analysis are shown in Figure 4.

| | Element, at. % | Al | Nb | Ti | V | Zr | Volume Fraction, % | Average Size, μm | |
|---|---|---|---|---|---|---|---|---|---|
| | | | | | | | | Transversal | Longitudinal |
| No. | Constituents Designation | | | | | | NbTiVZr | | |
| 1 | Light matrix | - | 45.5 | 5.8 | 46.0 | 2.7 | 46 ± 3 | 2.9 ± 1.5 | - |
| 2 | Grey phase | - | 7.5 | 10.4 | 2.2 | 79.9 | 35 ± 2 | 3.5 ± 1.6 | |
| 3 | Black phase | - | 9.2 | 77.2 | 8.8 | 4.8 | 19 ± 2 | 0.9 ± 0.3 | 3.2 ± 1.9 |
| | Alloy composition | - | 25.6 | 24.4 | 24.9 | 25.1 | - | - | |
| | | | | | | | $Al_{0.5}NbTiVZr$ | | |
| 1 | Matrix | 6.1 | 30.6 | 28.8 | 21.5 | 13.0 | 48 ± 3 | - | |
| 2 | Dark-grey particles | 16.8 | 14.1 | 10.8 | 28.9 | 29.4 | 39 ± 3 | 7.7 ± 4.5 (coarse); 1.8 ± 0.8 (fine) | |
| 3 | Light-grey particles | 17.7 | 12.4 | 16.6 | 16.1 | 37.2 | 13 ± 2 | 8.2 ± 3.0 | |
| | Alloy composition | 11.4 | 21.6 | 21.9 | 22.3 | 22.8 | - | - | |
| | | | | | | | AlNbTiVZr | | |
| 1 | Matrix | 12.7 | 27.8 | 28.8 | 24.8 | 5.9 | 52 ± 2 | - | |
| 2 | Dark-grey particles | 26.0 | 10.8 | 9.9 | 25.3 | 28.0 | 26 ± 3 | 5.0 ± 1.9 | 12.9 ± 6.3 |
| 3 | Light-grey particles | 35.4 | 12.7 | 10.8 | 3.9 | 37.2 | 22 ± 2 | 4.5 ± 1.3 | 8.1 ± 3.1 |
| | Alloy composition | 21.9 | 20.0 | 19.8 | 20.3 | 18.0 | - | - | |
| | | | | | | | $Al_{1.5}NbTiVZr$ | | |
| 1 | Dark phase | 23.6 | 19.8 | 25.2 | 16.3 | 5.1 | 36 ± 2 | - | |
| 2 | Dark-grey phase | 34.8 | 8.5 | 8.8 | 22.9 | 25.0 | 28 ± 3 | 2.9 ± 0.7 | 6.1 ± 2.8 |
| 3 | Light-grey phase | 39.3 | 13.1 | 9.7 | 4.3 | 33.6 | 16 ± 2 | 2.3±0.9 | |
| 4 | White phase | 31.8 | 30.2 | 16.8 | 9.6 | 11.6 | 20 ± 2 | 1.9 ± 0.8 | 4.5 ± 2.5 |
| | Alloy composition | 29.5 | 18.0 | 18.2 | 16.9 | 17.4 | - | - | |

### *3.3. Effect of Annealing at 800 °C on Structure of the $Al_xNbTiVZr$ ($x$ = 0; 0.5; 1; 1.5) Alloys*

The XRD patterns of the $Al_xNbTiVZr$ ($x$ = 0; 0.5; 1; 1.5) alloys after annealing at 800 °C are shown in Figure 5. The NbTiVZr alloy is composed of the same bcc, C15 Laves, and hcp phases as after annealing at 1000 °C (Figure 3). The $Al_{0.5}NbTiVZr$ alloy consists of bcc phase and C14 Laves phase. The AlNbTiVZr and $Al_{1.5}NbTiVZr$ alloys, in turn, are composed of bcc phase, C14 Laves phase and $Zr_2Al$-type phase. Several peaks from the $AlNb_2$-type phase are also found in the XRD pattern of the $Al_{1.5}NbTiVZr$ alloy.

Complex multiphase structure with noteworthy morphology is found in the NbTiVZr alloy after annealing at 800 °C (Figure 6a). Concentric circles formed by the second phase are found inside coarse matrix grains (marked as point 1 in Figure 6a). The circles are formed mostly of grey phase (marked as point 2). The same grey phase is found on matrix grain boundaries. The width of the second grey phase circular layers is ≈3 μm. Additional black phase (high magnification insert in Figure 6a) is present inside or adjacent grey phase particles. Black particles have complex irregular shape and characteristic dimensions around 1 μm. EBSD shows that the matrix has bcc structure, dark-grey phase—hcp structure, and black phase has (ordered) fcc structure. Examinations of the chemical composition of other constitutive phases have revealed that the light matrix composed mostly of Nb, Ti and V but almost does not contain any Zr while the dark-grey hcp phase consists primary of Zr (Table 3). The black phase is enriched with Ti and Zr and depleted of Nb and V. Volume fractions of light bcc matrix, dark-grey hcp phase and black C15 fcc Laves phase are, respectively, 46%, 37% and 17%.

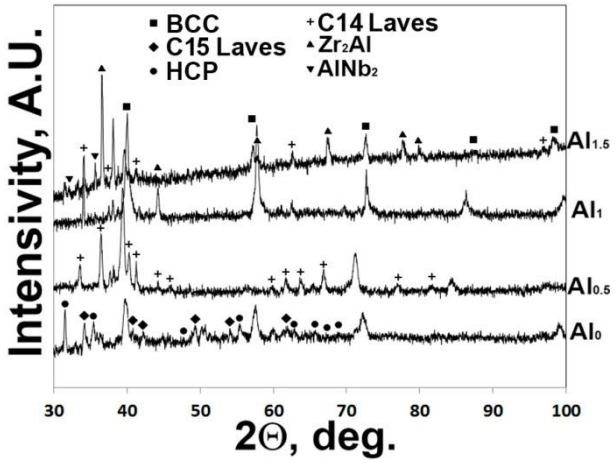


**Figure 5.** XRD patterns of the $Al_xNbTiVZr$ ($x$ = 0; 0.5; 1; and 1.5) alloys after annealing at 800 °C for 100 h.

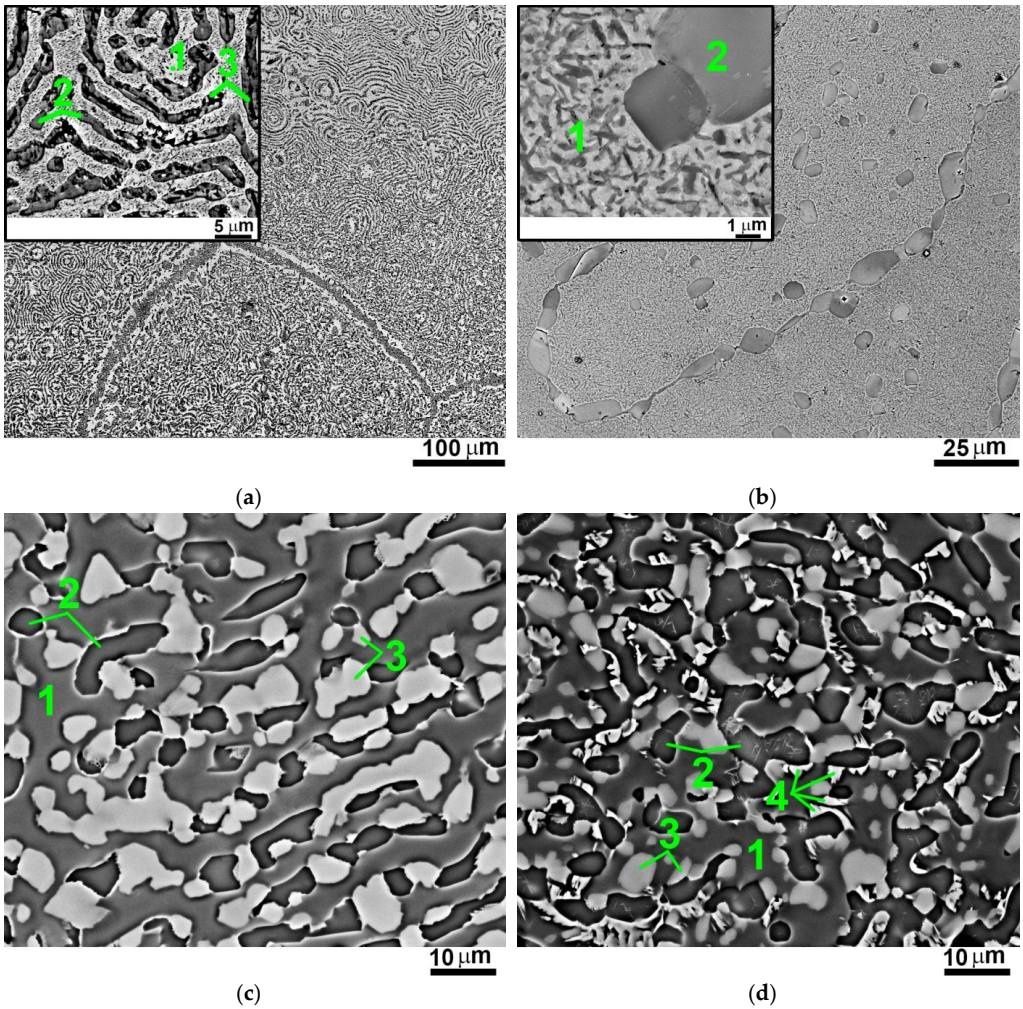


**Figure 6.** SEM-BSE images of the microstructures of the $Al_xNbTiVZr$ ($x$ = 0 (**a**); 0.5 (**b**); 1 (**c**); 1.5 (**d**)) alloys after annealing at 800 °C for 100 h. Chemical compositions and volume fractions of the numbered constituents are given in Table 3.

**Table 3.** Chemical compositions, volume fractions and dimensions of the constituents of the $Al_xNbTiVZr$ ($x$ = 0; 0.5; 1; 1.5) alloys after annealing at 800 °C for 100 h. Typical regions used for analysis are shown in Figure 6.

| | Element, at. % | Al | Nb | Ti | V | Zr | Volume Fraction, % | Average Size, μm | |
|---|---|---|---|---|---|---|---|---|---|
| | | | | | | | | Transversal | Longitudinal |
| No. | Constituents Designation | | | | | | NbTiVZr | | |
| 1 | Light matrix | - | 33.0 | 29.5 | 35.0 | 2.5 | 46 ± 3 | 2.8 ± 1.9 | >100 |
| 2 | Grey phase | - | 9.3 | 7.5 | 12.3 | 70.9 | 37 ± 3 | 2.9 ± 1.7 | >100 |
| 3 | Black phase | - | 5.3 | 56.4 | 2.6 | 35.7 | 17 ± 2 | 1.0 ± 0.4 | 2.3 ± 1.2 |
| | Alloy composition | - | 25.6 | 24.4 | 24.9 | 25.1 | - | - | |
| | | | | | | | $Al_{0.5}NbTiVZr$ | | |
| 1 | Decomposed matrix | 9.6 | 24.4 | 25.6 | 20.7 | 19.7 | 87 ± 3 [1] | - | |
| 2 | Grey particles | 16.3 | 13.3 | 11.8 | 27.8 | 30.8 | 13 ± 1 | 6.8 ± 3.5 | |
| | Alloy composition | 11.4 | 21.6 | 21.9 | 22.3 | 22.8 | - | - | |
| | | | | | | | AlNbTiVZr | | |
| 1 | Matrix | 16.4 | 27.0 | 24.0 | 27.6 | 5.0 | 54 ± 3 | - | |
| 2 | Dark-grey particles | 30.6 | 9.3 | 7.6 | 24.3 | 28.2 | 16 ± 2 | 3.3 ± 1.0 | 7.3 ± 3.2 |
| 3 | Light-grey particles | 36.7 | 13.4 | 9.3 | 4.5 | 36.1 | 30 ± 3 | 3.3 ± 1.2 | 5.7 ± 3.1 |
| | Alloy composition | 21.9 | 20.0 | 19.8 | 20.3 | 18.0 | - | - | |
| | | | | | | | $Al_{1.5}NbTiVZr$ | | |
| 1 | Matrix | 24.9 | 24.3 | 26.0 | 17.3 | 7.5 | 46 ± 2 | - | |
| 2 | Dark-grey particles | 34.8 | 9.6 | 8.0 | 20.9 | 26.7 | 29 ± 3 | 3.4 ± 1.4 | 9.6 ± 5.2 |
| 3 | Light-grey particles | 38.1 | 13.6 | 11.1 | 5.3 | 31.9 | 18 ± 2 | 3.2 ± 1.5 | |
| 4 | White particles | 32.7 | 32.8 | 16.4 | 9.9 | 8.2 | 7 ± 1 | 1.2 ± 0.5 | 4.3 ± 2.5 |
| | Alloy composition | 29.5 | 18.0 | 18.2 | 16.9 | 17.4 | - | - | |

[1] The volume fraction of dark particles inside decomposed matrix is 37 ± 3%.

Microstructure of the $Al_{0.5}NbTiVZr$ alloy after 800 °C annealing (Figure 6b) is composed of coarse Laves phase particles (marked with point 2 in Figure 6b), inherited from high temperature annealed condition, and fine dual-phase matrix structure, most likely produced by decomposition of initial bcc matrix phase (marked as point 1). The volume fraction of dark fine Laves phase particles in decomposed matrix is 37%. The chemical composition of the constitutive phases (Table 3) is similar to that after high temperature annealing (Table 1).

The structure of the AlNbTiVZr alloy after exposure at 800 °C (Figure 6c) is similar to the structure of the alloy after higher temperatures annealing (Figures 2c and 4c) and is composed of bcc matrix (marked with point 1 in Figure 6c) with dark-grey Laves phase (marked with point 2) and light-grey $Zr_2Al$-type phase (marked with point 3) particles. However, the changes in volume fraction of constituents and their chemical composition have to be noted (Table 3). For example, the volume fraction of light-grey particles of $Zr_2Al$-type phase increases to 30%, and concentration of Zr in bcc matrix decreases to 5.0%.

The microstructure of the $Al_{1.5}NbTiVZr$ alloy after annealing at 800 °C for 100 hours (Figure 6d) resembles the microstructure of the sample after annealing at 1000 °C (Figure 4d). The structure is also composed of four structural constituents—bcc matrix (marked with point 1 in Figure 6d) with dark-grey Laves phase (marked with point 2), light-grey $Zr_2Al$-type phase (marked with point 3) and white $AlNb_2$-type sigma phase particles (marked with point 4). The volume fraction of the $AlNb_2$-type particles is 7% and the volume fraction of $Zr_2Al$-type particles is 18% (Table 3). The chemical composition of the constitutive phases is similar to that after annealing at 1000 °C (Table 2).

## 4. Discussion

The results of the structural observations of the $Al_xNbTiVZr$ ($x$ = 0; 0.5; 1; 1.5) alloys after annealing at 800–1200 °C (Figures 1–6, Tables 1–3) shows that both Al content and annealing temperature have

pronounced effects on resulting phase composition of the alloys. To summarize, the constitutive phases of the alloys in different conditions and their volume fractions are shown in Figure 7. Apparently, after annealing at high temperature of 1200 °C, the increase of Al content results in formation of intermetallic second phases: they are absent in the bcc-structured NbTiVZr alloy, and the Al-containing alloys contain C14 Laves phase and $Zr_2Al$-type phases with aggregate volume fraction proportional to Al concentration. Subsequent annealing at intermediate temperatures of 800 °C and 1000 °C results in formation of additional second phases in the $Al_x$NbTiVZr alloys. The most significant changes are observed in the NbTiVZr alloy: it is composed of bcc matrix, hexagonal Zr-based solid solution phase and C15 Laves phase particles after intermediate temperature annealing. In the $Al_{0.5}$NbTiVZr alloy, the volume fraction of C14 Laves phase increases considerably, most probably as the result of decomposition of bcc solid solution. The weakest changes due to intermediate temperature annealing are found in the AlNbTiVZr alloy, where only pronounced increase of $Zr_2Al$-type particles has to be noted. In the $Al_{1.5}$NbTiVZr alloy, new $AlNb_2$-type phase appears after annealing. Note that the annealing temperature (800 °C or 1000 °C) does not affect the fractions of the observed phases noticeably.

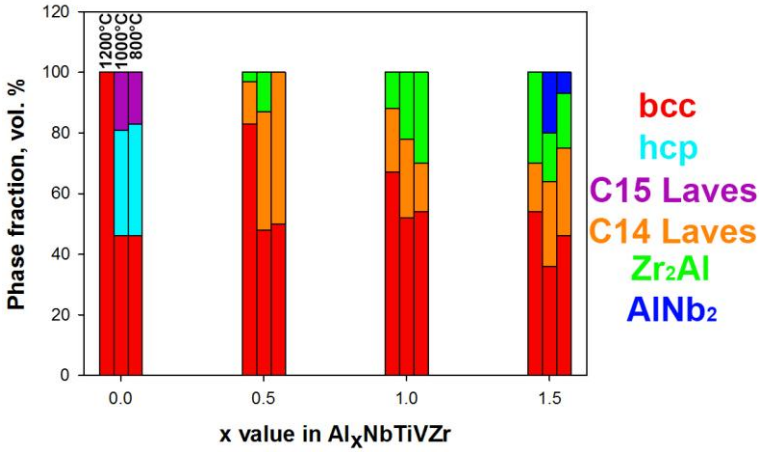


**Figure 7.** Fractions of the constitutive phases of the $Al_x$NbTiVZr ($x$ = 0; 0.5; 1; 1.5) alloys after annealing at 1200 °C for 24 h and at 800 °C and 1000 °C for 100 h.

Many efforts have been devoted to prediction of solid solution or intermetallic phase formation in HEAs [36–44]. In previous work, the phase composition of the as-solidified or high temperature annealed $Al_x$NbTiVZr alloys was analyzed using existing criteria for solid solution/intermetallic phase formation with limited successes [27]. Here, we have used approach proposed in [45]. The basic idea of this approach is that the free energy of the solid solution phase have to be compared with enthalpies of formations of possible intermetallic phases, i.e., Gibbs free energies of the different possible phases have to be compared to identify the thermodynamically stable phase at given temperature. The condition for suppression of intermetallic (IM) phases at a temperature $T$ is defined as:

$$k_1{}^{cr}(T) > \Delta H_{IM}/\Delta H_{mix} \quad (1)$$

where $k_1{}^{cr}(T) = 1 + ((T\Delta S_{mix})(1 - k_2))/|\Delta H_{mix}|$ ($k_1{}^{cr}$ is calculated for a partially ordered condition of an IM phase ($k_2$ = 0.6)); $\Delta H_{IM} = \sum_{(I<y)} 4H_{ij}{}^{IM}c_ic_j$ and $\Delta H_{mix} = \sum_{(i<y)} 4H_{ij}{}^{mix}c_ic_j$—enthalpies of mixing for IM and solid solution (SS) phases (the enthalpy of formation values $H_{ij}{}^{IM}$ for binary IM and $H_{ij}{}^{mix}$ for elements i and j are reported in [46] and [47], respectively). Respectively, the alloys with $k_1{}^{cr}$ $(T) < \Delta H_{IM}/\Delta H_{mix}$ are expected to contain IM phases in addition to SS phases. We have calculated the $k_1{}^{cr}(T)$ and $\Delta H_{IM}/\Delta H_{mix}$ according to the formulae above, and the predicted equilibrium phases (SS or SS + IM) in the $Al_x$NbTiVZr ($x$ = 0; 0.5; 1; 1.5) alloys at 800 °C, 1000 °C and 1200 °C are listed in Table 4.

**Table 4.** Calculated $k_1{}^{cr}(T)$ and $\Delta H_{IM}/\Delta H_{mix}$ parameters and predicted phases for the $Al_xNbTiVZr$ ($x$ = 0; 0.5; 1; 1.5) alloys at 800 °C, 1000 °C and 1200 °C.

| Temperature, °C | Alloy | $k_1{}^{cr}(T)$ | $\Delta H_{IM}/\Delta H_{mix}$ | Predicted Phase Composition |
|---|---|---|---|---|
| 800 | NbTiVZr | 19.79 | −6.08 | SS |
| | $Al_{0.5}NbTiVZr$ | 0.52 | 1.24 | SS + IM |
| | AlNbTiVZr | 0.33 | 1.31 | SS + IM |
| | $Al_{1.5}NbTiVZr$ | 0.27 | 1.33 | SS + IM |
| 1000 | NbTiVZr | 23.48 | −6.08 | SS |
| | $Al_{0.5}NbTiVZr$ | 0.62 | 1.24 | SS + IM |
| | AlNbTiVZr | 0.39 | 1.31 | SS + IM |
| | $Al_{1.5}NbTiVZr$ | 0.31 | 1.33 | SS + IM |
| 1200 | NbTiVZr | 27.16 | −6.08 | SS |
| | $Al_{0.5}NbTiVZr$ | 0.72 | 1.24 | SS + IM |
| | AlNbTiVZr | 0.45 | 1.31 | SS + IM |
| | $Al_{1.5}NbTiVZr$ | 0.36 | 1.33 | SS + IM |

Table 4 shows that the $k_1{}^{cr}(T) > \Delta H_{IM}/\Delta H_{mix}$ criterion can correctly predict high temperature phases of the studied $Al_xNbTiVZr$ alloys, i.e., it predicts formation of IM phases in the Al-containing $Al_xNbTiVZr$ alloys after annealing at 1200 °C. The decrease of the $k_1{}^{cr}(T)$ values and the increase of the $\Delta H_{IM}/\Delta H_{mix}$ values in the Al-containing $Al_xNbTiVZr$ alloys can be attributed to strong chemical affinity between Al and Zr, ($\Delta H^{mix}{}_{Al\text{-}Zr} = -44$ kJ/mol [47]) and high negative enthalpy of formation of intermetallics in the respective pair ($\Delta H^{IM}{}_{Al\text{-}Zr} \approx -52$ kJ/mol [46]). Therefore, it can be concluded that strong interaction between the Al and Zr atoms govern intermetallic phase formation in the $Al_xNbTiVZr$ alloys at high temperatures. This conclusion is supported by the results of chemical analysis (Table 1), which shows that the second phases in the Al-containing $Al_xNbTiVZr$ alloys after annealing at 1200 °C are mostly composed of Al and Zr. However, the $k_1{}^{cr}(T)$ and $\Delta H_{IM}/\Delta H_{mix}$ values calculated at 800 °C and 1000 °C are almost identical to that at 1200 °C, i.e., drastic structural changes (Figure 7) after intermediate temperature annealing cannot be predicted according to the $k_1{}^{cr}(T) > \Delta H_{IM}/\Delta H_{mix}$ criterion. The reasons for such changes will be discussed further.

Analysis of the data on the chemical composition of the constitutive phases of the $Al_xNbTiVZr$ alloys shows that: (i) after annealing at 800 °C and 1000 °C, the content of Zr in the bcc phase becomes much smaller in comparison with the bcc phase after annealing at 1200 °C (Tables 1–3); and (ii) the second phases formed after intermediate temperature annealing are generally enriched with Zr (this is especially true in the case of the NbTiVZr and $Al_{0.5}NbTiVZr$ alloys) (Tables 1–3). It might seem that the more significant changes in Zr concentration in the bcc phase are found, the higher is the amount of second phases appeared after annealing at 800 °C or 1000 °C. To prove this assumption, the dependence of increase of volume fraction of second phases, $dV_{SP}$, calculated as the difference between the aggregate volume fraction of second phases in the alloy in high (1200 °C) temperature annealed condition, and the aggregate volume fraction of second phases found after annealing at 800 °C or 1000 °C, on decrease of Zr concentration in the bcc matrix, $dC_{Zr}$, calculated as the difference between the Zr concentration in bcc phase in the alloy after annealing at 1200 °C, and the Zr concentration in bcc phase after intermediate temperature annealing, was calculated and plotted in Figure 8.

The $dV_{SP}$ vs. $dC_{Zr}$ plot (Figure 8) shows almost linear dependence of $dV_{SP}$ on $dC_{Zr}$. It means that formation of second phases after annealing at 800 °C and 1000 °C is associated with depletion of bcc phase with Zr. It might be supposed that Zr atoms solubility in the bcc phase of the $Al_xNbTiVZr$ alloys decreases at intermediate temperature. Decrease of solubility of alloying elements in equilibrium solid solution with decrease of a temperature is a common phenomenon. Zr has highest atomic radius among the constitutive elements of the system (160 pm), and one of the lowest shear modulus (33 GPa) (the information on other constitutive elements can be found in Table 5 of [27]). The allotropic bcc-to-hcp transformation exhibited by pure Zr at temperature of 863 °C also has to be noted. Therefore, it is likely that Zr is repulsed from equilibrium intermediate-temperature bcc phase of the $Al_xNbTiVZr$ alloys. The slope of the dashed line in Figure 8 implies, that per 1 at. % of Zr concentration in bcc

matrix decrease, the volume fraction of second phases increase by 2.5%. Therefore, the higher is amount of Zr in the equilibrium high temperature bcc phase of the $Al_xNbTiVZr$ alloys, the higher amount of second phases appears after annealing at lower temperatures.

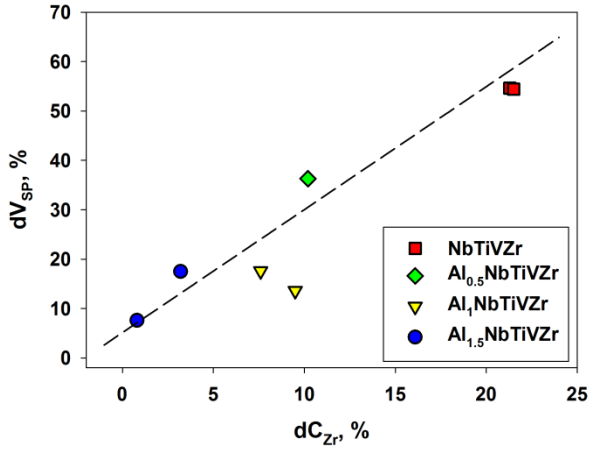


**Figure 8.** The dependence between the increase of second phase volume fraction ($dV_{SP}$) and the decrease of the Zr content in the bcc solid solution phase due to intermediate temperature (800 °C and 1000 °C) annealing ($dC_{Zr}$) in the $Al_xNbTiVZr$ ($x$ = 0; 0.5; 1; 1.5) alloys.

The nature of the second phases that are formed in the $Al_xNbTiVZr$ alloys after annealing at 800 °C or 1000 °C is dependent on chemical composition of the alloys. With increase of Al content, $x$, the sequence of precipitation during annealing at 800 °C and 1000 °C phases can be described as: hcp Zr-rich phase ($x$ = 0), C14 Laves phase ($x$ = 0.5), $Zr_2Al$-type phase ($x$ = 1) and $AlNb_2$-type phase ($x$ = 1.5). Obviously, the precipitated second phases tend to contain less Zr and more Al with increase of Al concentration in the $Al_xNbTiVZr$ alloys. The obtained results give suggestions on solvus temperatures of some phases; for example, the hcp Zr-rich phase and C15 Laves phase in the NbTiVZr alloy and $AlNb_2$-type phase in the $Al_{1.5}NbTiVZr$ alloys likely have the solvus temperatures in the 1000–1200 °C interval. It should also be mentioned that formation of $AlNb_2$-type phase and changes of volume fractions of constitutive phases in $Al_{1.5}NbTiVZr$ alloy cannot be associated solely with decrease of Zr concentration in the bcc phase; in this case, probably, complex redistribution of alloying elements between the constitutive phases is responsible for the observed transformations.

The complex, circular microstructure found in the NbTiVZr alloy after annealing at 800 °C deserves additional attention. It is likely that such structure can be produced by complex phase transformations. Investigation of the structure of the alloy after compression deformation at 800 °C and 1000 °C [48] has shown presence of bcc and C14 (hexagonal) Laves phases. Therefore, it might be assumed that decomposition of high-temperature bcc solid solution phase at 800–1000 °C involves formation of intermediate C14 Laves phase, which further decomposes into Zr-rich hcp phase and C15 Laves phase. Probably, this sequence of phase transformations is responsible for the complex morphology of the structure of the NbTiVZr alloy after annealing at 800 °C. However, additional investigations are required to verify the exact sequence of phase transformations in the alloy and their mechanisms.

In summary, the presented results show that second (mostly, intermetallic) phase formation in the $Al_xNbTiVZr$ alloys is governed by different factors at respectively high (1200 °C) and intermediate (800 °C and 1000 °C) temperatures: by strong chemical affinity and high enthalpy of intermetallic phases formation in the Al-Zr atomic pair at high temperatures; and by poor "compatibility" of Zr atoms with other components of the bcc solid solution phase at lower temperatures. As the result, at high temperatures, the Al-free NbTiVZr alloy has single bcc phase structure, while in the Al-containing alloys intermetallic phases are observed. On the other hand, at intermediate temperature

the high-temperature bcc solid solution of the NbTiVZr alloy decomposes with formation of large fraction of second phases, and the alloys containing high amounts of Al (like the AlNbTiVZr alloy) remain relatively stable as Zr in these alloys is already found predominantly in second intermetallic phases. Current results also show that the ability to form single solid solution phase at high temperature does not imply the stability of this phase at lower temperatures. This aspect has to be considered, especially in development of HEAs suitable for high-temperature applications.

## 5. Conclusions

In the present study, the structure of the $Al_x$NbTiVZr ($x$ = 0; 0.5; 1; 1.5) high entropy alloys after annealing at 1200 °C for 24 h and subsequent annealing at 800 °C and 1000 °C for 100 h are examined. Following conclusions are drawn:

(1) The structure of the $Al_x$NbTiVZr ($x$ = 0; 0.5; 1; 1.5) alloys after annealing at 1200 °C strongly depends on Al content. The NbTiVZr alloy has single bcc phase structure, while in the Al-containing alloys, C14 Laves and $Zr_2Al$-type phases are found. The aggregate volume fraction of second phases increases with increase of Al content from 17% of the $Al_{0.5}$NbTiVZr alloy to 46% of the $Al_{1.5}$NbTiVZr alloy. The C14 Laves and $Zr_2Al$-type phases are mostly composed of Zr and Al.

(2) Annealing at lower temperatures of 800 °C and 1000 °C results in formation of additional second phases in the $Al_x$NbTiVZr alloys. The amount and nature of second phases almost does not depend on annealing temperature (800 °C or 1000 °C) but strongly depends on the Al content in the alloy:

   a. in the NbTiVZr alloy, additional Zr-rich hcp and C15 Laves phases appear;
   b. in the $Al_{0.5}$NbTiVZr alloy, the amount of C14 Laves phase increases substantially;
   c. in the AlNbTiVZr alloy, the amount of $Zr_2Al$-type phase increases; and
   d. in the $Al_{1.5}$NbTiVZr alloy, additional $AlNb_2$-type phase appears.

(3) The highest amount of second phases appeared after annealing at 800 °C and 1000 °C is found in the NbTiVZr alloy (54%), and the lowest amount (7.6% to 17.6%) is found in the AlNbTiVZr and $Al_{1.5}$NbTiVZr alloys.

(4) The analysis has revealed that the formation of second (intermetallic) phases in the $Al_x$NbTiVZr ($x$ = 0; 0.5; 1; 1.5) alloys after annealing at 1200 °C can be associated with strong chemical affinity and highly negative mixing enthalpy in Al-Zr atomic pair. At lower temperatures of 800 °C and 1000 °C, formation of second phases is mostly associated with decrease of Zr solubility in the bcc solid solution phase.

**Acknowledgments:** The authors gratefully acknowledge the financial support from the Russian Science Foundation Grant No. 14-19-01104. The authors are grateful to the personnel of the Joint Research Centre, Belgorod State University, for their assistance with the instrumental analysis.

**Author Contributions:** N.D.S. and G.A.S. conceived and designed the experiments; M.A.T. prepared the experimental alloys, N.Y.Y. performed the experiments; N.Y.Y. and N.D.S. analyzed the data; and N.D.S. and G.A.S. wrote the paper.

**Conflicts of Interest:** The authors declare no conflict of interest. The founding sponsors had no role in the design of the study; in the collection, analyses, or interpretation of data; in the writing of the manuscript, and in the decision to publish the results.

## References

1. Zhang, Y.; Zuo, T.T.; Tang, Z.; Gao, M.C.; Dahmen, K.A.; Liaw, P.K.; Lu, Z.P. Microstructures and properties of high-entropy alloys. *Prog. Mater. Sci.* **2014**, *61*, 1–93. [CrossRef]
2. Yeh, J.W.; Chen, S.K.; Lin, S.J.; Gan, J.Y.; Chin, T.S.; Shun, T.T.; Tsau, C.H.; Chang, S.Y. Nanostructured High-Entropy Alloys with Multiple Principal Elements: Novel Alloy Design Concepts and Outcomes. *Adv. Eng. Mater.* **2004**, *6*, 299–303. [CrossRef]

3. Zhou, Y.J.; Zhang, Y.; Wang, Y.L.; Chen, G.L. Solid solution alloys of $AlCoCrFeNiTi_x$ with excellent room-temperature mechanical properties. *Appl. Phys. Lett.* **2007**, *90*, 181904. [CrossRef]
4. Youssef, K.M.; Zaddach, A.J.; Niu, C.; Irving, D.L.; Koch, C.C. A novel low-density, high-hardness, high-entropy alloy with close-packed single-phase nanocrystalline structures. *Mater. Res. Lett.* **2015**, *3*, 95–99. [CrossRef]
5. He, J.Y.; Wang, H.; Huang, H.L.; Xu, X.D.; Chen, M.W.; Wu, Y.; Liu, X.J.; Nieh, T.G.; An, K.; Lu, Z.P. A precipitation-hardened high-entropy alloy with outstanding tensile properties. *Acta Mater.* **2016**, *102*, 187–196. [CrossRef]
6. Gludovatz, B.; Hohenwarter, A.; Catoor, D.; Chang, E.H.; George, E.P.; Ritchie, R.O. A fracture-resistant high-entropy alloy for cryogenic applications. *Science* **2014**, *345*, 1153–1158. [CrossRef] [PubMed]
7. Gludovatz, B.; Hohenwarter, A.; Thurston, K.V.; Bei, H.; Wu, Z.; George, E.P.; Ritchie, R.O. Exceptional damage-tolerance of a medium-entropy alloy CrCoNi at cryogenic temperatures. *Nat. Commun.* **2016**, *7*, 10602. [CrossRef] [PubMed]
8. Li, D.; Zhang, Y. The ultrahigh charpy impact toughness of forged $Al_xCoCrFeNi$ high entropy alloys at room and cryogenic temperatures. *Intermetallics* **2016**, *70*, 24–28. [CrossRef]
9. Chuang, M.H.; Tsai, M.H.; Wang, W.R.; Lin, S.J.; Yeh, J.W. Microstructure and wear behavior of $Al_xCo_{1.5}CrFeNi_{1.5}Ti_y$ high-entropy alloys. *Acta Mater.* **2011**, *59*, 6308–6317. [CrossRef]
10. Miracle, D.B.; Miller, J.D.; Senkov, O.N.; Woodward, C.; Uchic, M.D.; Tiley, J. Exploration and development of high entropy alloys for structural applications. *Entropy* **2014**, *16*, 494–525. [CrossRef]
11. Daoud, H.M.; Manzoni, A.M.; Wanderka, N.; Glatzel, U. High-Temperature Tensile Strength of $Al_{10}Co_{25}Cr_8Fe_{15}Ni_{36}Ti_6$ Compositionally Complex Alloy (High-Entropy Alloy). *JOM* **2015**, *67*, 2271–2277. [CrossRef]
12. Senkov, O.N.; Senkova, S.V.; Miracle, D.B.; Woodward, C. Mechanical properties of low-density, refractory multi-principal element alloys of the Cr–Nb–Ti–V–Zr system. *Mater. Sci. Eng. A* **2013**, *565*, 51–62. [CrossRef]
13. Senkov, O.N.; Woodward, C.; Miracle, D.B. Microstructure and properties of aluminum-containing refractory high-entropy alloys. *JOM* **2014**, *66*, 2030–2042. [CrossRef]
14. Stepanov, N.D.; Yurchenko, N.Y.; Skibin, D.V.; Tikhonovsky, M.A.; Salishchev, G.A. Structure and mechanical properties of the $AlCr_xNbTiV$ ($x$ = 0, 0.5, 1, 1.5) high entropy alloys. *J. Alloy. Compd.* **2015**, *652*, 266–280. [CrossRef]
15. Stepanov, N.D.; Yurchenko, N.Y.; Sokolovsky, V.S.; Tikhonovsky, M.A.; Salishchev, G.A. An $AlNbTiVZr_{0.5}$ high-entropy alloy combining high specific strength and good ductility. *Mater. Lett.* **2015**, *16*, 136–139. [CrossRef]
16. Senkov, O.N.; Wilks, G.B.; Miracle, D.B.; Chuang, C.P.; Liaw, P.K. Refractory high-entropy alloys. *Intermetallics* **2010**, *18*, 1758–1765. [CrossRef]
17. Senkov, O.N.; Wilks, G.B.; Scott, J.M.; Miracle, D.B. Mechanical properties of $Nb_{25}Mo_{25}Ta_{25}W_{25}$ and $V_{20}Nb_{20}Mo_{20}Ta_{20}W_{20}$ refractory high entropy alloys. *Intermetallics* **2011**, *19*, 698–706. [CrossRef]
18. Senkov, O.N.; Scott, J.M.; Senkova, S.V.; Miracle, D.B.; Woodward, C.F. Microstructure and room temperature properties of a high-entropy TaNbHfZrTi alloy. *J. Alloy. Compd.* **2011**, *509*, 6043–6048. [CrossRef]
19. Senkov, O.N.; Scott, J.M.; Senkova, S.V.; Meisenkothen, F.; Miracle, D.B.; Woodward, C.F. Microstructure and elevated temperature properties of a refractory TaNbHfZrTi alloy. *J. Mater. Sci.* **2012**, *47*, 4062–4074. [CrossRef]
20. Senkov, O.N.; Woodward, C.F. Microstructure and properties of a refractory $CrNbMo_{0.5}Ta_{0.5}TiZr$ alloy. *Mater. Sci. Eng. A* **2011**, *529*, 311–320. [CrossRef]
21. Senkov, O.N.; Senkova, S.V.; Woodward, C.; Miracle, D.B. Low-density, refractory multi-principal element alloys of the Cr–Nb–Ti–V–Zr system: Microstructure and phase analysis. *Acta Mater.* **2013**, *61*, 1545–1557. [CrossRef]
22. Wu, Y.D.; Cai, Y.H.; Chen, X.H.; Wang, T.; Si, J.J.; Wang, L.; Wang, Y.D.; Hui, X.D. Phase composition and solid solution strengthening effect in TiZrNbMoV high-entropy alloys. *Mater. Des.* **2015**, *83*, 651–660. [CrossRef]
23. Guo, N.N.; Wang, L.; Luo, L.S.; Li, X.Z.; Su, Y.Q.; Guo, J.J.; Fu, H.Z. Microstructure and mechanical properties of refractory MoNbHfZrTi high-entropy alloy. *Mater. Des.* **2015**, *81*, 87–94. [CrossRef]
24. Czerwinski, F.; Jochym, P.T.; Litynska-Dobrzynska, L. Microstructure and mechanical properties of the novel $Hf_{25}Sc_{25}Ti_{25}Zr_{25}$ equiatomic alloy with hexagonal solid solutions. *Mater. Des.* **2016**, *92*, 8–17. [CrossRef]

25. Senkov, O.N.; Senkova, S.V.; Woodward, C. Effect of aluminum on the microstructure and properties of two refractory high-entropy alloys. *Acta Mater.* **2014**, *68*, 214–228. [CrossRef]
26. Stepanov, N.D.; Shaysultanov, D.G.; Salishchev, G.A.; Tikhonovsky, M.A. Structure and mechanical properties of a light-weight AlNbTiV high entropy alloy. *Mater. Lett.* **2015**, *142*, 153–155. [CrossRef]
27. Stepanov, N.D.; Yurchenko, N.Y.; Shaysultanov, D.G.; Salishchev, G.A.; Tikhonovsky, M.A. Effect of Al on structure and mechanical properties of $Al_xNbTiVZr$ ($x$ = 0, 0.5, 1, 1.5) high entropy alloys. *Mater. Sci. Technol.* **2015**, *31*, 1184–1193. [CrossRef]
28. Lin, C.M.; Juan, C.C.; Chang, C.H.; Tsai, C.W.; Yeh, J.W. Effect of Al addition on mechanical properties and microstructure of refractory $Al_xHfNbTaTiZr$ alloys. *J. Alloy. Compd.* **2015**, *624*, 100–107. [CrossRef]
29. Poletti, M.G.; Fiore, G.; Szost, B.A.; Battezzati, L. Search for high entropy alloys in the X-NbTaTiZr systems (X = Al, Cr, V, Sn). *J. Alloy. Compd.* **2015**, *620*, 283–288. [CrossRef]
30. Poletti, M.G.; Branz, S.; Fiore, G.; Szost, B.A.; Crichton, W.A.; Battezzati, L. Equilibrium high entropy phases in X-NbTaTiZr (X = Al, V, Cr and Sn) multiprincipal component alloys. *J. Alloy. Compd.* **2016**, *655*, 138–146. [CrossRef]
31. Gorr, B.; Azim, M.; Christ, H.J.; Mueller, T.; Schliephake, D.; Heilmaier, M. Phase equilibria, microstructure, and high temperature oxidation resistance of novel refractory high-entropy alloys. *J. Alloy. Compd.* **2015**, *624*, 270–278. [CrossRef]
32. Yurchenko, N.Y.; Stepanov, N.D.; Shaysultanov, D.G.; Tikhonovsky, M.A.; Salishchev, G.A. Effect of Al content on structure and mechanical properties of the $Al_xCrNbTiVZr$ ($x$ = 0; 0.25; 0.5; 1) high-entropy alloys. *Mater. Charact.* **2016**, *121*, 125–134. [CrossRef]
33. Chen, H.; Kauffmann, A.; Gorr, B.; Schliephake, D.; Seemüller, C.; Wagner, J.N.; Christ, H.J.; Heilmaier, M. Microstructure and mechanical properties at elevated temperatures of a new Al-containing refractory high-entropy alloy Nb-Mo-Cr-Ti-Al. *J. Alloy. Compd.* **2016**, *661*, 206–215. [CrossRef]
34. Gorr, B.; Azim, M.; Christ, H.J.; Chen, H.; Szabo, D.V.; Kauffmann, A.; Heilmaier, M. Microstructure Evolution in a New Refractory High-Entropy Alloy W-Mo-Cr-Ti-Al. *Met. Mater. Trans. A* **2016**, *47*, 961–970. [CrossRef]
35. Fazakas, E.; Zadorozhnyy, V.; Varga, L.K.; Inoue, A.; Louzguine-Luzgin, D.V.; Tian, F.; Vitos, L. Experimental and theoretical study of $Ti_{20}Zr_{20}Hf_{20}Nb_{20}X_{20}$ (X = V or Cr) refractory high-entropy alloys. *Int. J. Refract. Met. H* **2014**, *47*, 131–138. [CrossRef]
36. Zhang, Y.; Zhou, Y.J.; Lin, J.P.; Chen, G.L.; Liaw, P.K. Solid-Solution Phase Formation Rules for Multi-component Alloys. *Adv. Eng. Mater.* **2008**, *10*, 534–538. [CrossRef]
37. Guo, S.; Ng, C.; Lu, J.; Liu, C.T. Effect of valence electron concentration on stability of fcc or bcc phase in high entropy alloys. *J. Appl. Phys.* **2011**, *109*, 103505. [CrossRef]
38. Guo, S.; Liu, C.T. Phase stability in high entropy alloys: Formation of solid-solution phase or amorphous phase. *Prog. Nat. Sci. Mater. Int.* **2011**, *21*, 433–446. [CrossRef]
39. Yang, X.; Zhang, Y. Prediction of high-entropy stabilized solid-solution in multi-component alloys. *Mater. Chem. Phys.* **2012**, *132*, 233–238. [CrossRef]
40. Tsai, M.H.; Tsai, K.Y.; Tsai, C.W.; Lee, C.; Juan, C.C.; Yeh, J.W. Criterion for Sigma Phase Formation in Cr- and V-Containing High-Entropy Alloys. *Mater. Res. Lett.* **2013**, *1*, 207–212. [CrossRef]
41. Poletti, M.G.; Battezzati, L. Electronic and thermodynamic criteria for the occurrence of high entropy alloys in metallic systems. *Acta Mater.* **2014**, *74*, 297–306. [CrossRef]
42. Dong, Y.; Lu, Y.; Jiang, L.; Wang, T.; Li, T. Effects of electro-negativity on the stability of topologically close-packed phase in high entropy alloys. *Intermetallics* **2014**, *52*, 105–109. [CrossRef]
43. Yurchenko, N.; Stepanov, N.; Salishchev, G. Laves-phase formation criterion for high-entropy alloys. *Mater. Sci. Technol.* **2016**, 1–6. [CrossRef]
44. Zhang, Y.; Guo, S.; Liu, C.T.; Yang, X. Phase formation rules. In *High Entropy Alloys: Fundamentals and Applications*; Gao, M.C., Yeh, J.W., Liaw, P.K., Zhang, Y., Eds.; Springer International Publishing: Basel, Switzerland, 2016; pp. 21–49.
45. Senkov, O.N.; Miracle, D.B. A New Thermodynamic Parameter to Predict Formation of Solid Solution or Intermetallic Phases in High Entropy Alloys. *J. Alloy. Compd.* **2016**, *658*, 603–607. [CrossRef]
46. Troparevsky, M.C.; Morris, J.R.; Kent, P.R.C.; Lupini, A.R.; Stocks, G.M. Criteria for Predicting the Formation of Single-Phase High-Entropy Alloys. *Phys. Rev. X* **2015**, *5*, 011041. [CrossRef]

47. Takeuchi, A.; Inoue, A. Classification of Bulk Metallic Glasses by Atomic Size Difference, Heat of Mixing and Period of Constituent Elements and Its Application to Characterization of the Main Alloying Element. *Mater. Trans. JIM* **2005**, *46*, 2817–2829. [CrossRef]
48. Yurchenko, N.Y.; Stepanov, N.D.; Shaysultanov, D.G.; Tikhonovsky, M.A.; Salishchev, G.A. Elevated temperature mechanical properties of the $Al_xNbTiVZr$ ($x$ = 0; 0.5; 1; 1.5) high entropy alloys. Manuscript in preparation.